Response from authors

Re: Review of WRF-GC (v2.0): online two-way coupling of WRF (v3.9.1.1) and GEOS-Chem (v12.7.2) for modeling regional atmospheric chemistry-meteorology interactions

May 10, 2021

We thank the three Reviewers for their helpful comments. In response, we made the following major changes: (1) expanded the analyses on the impacts of ARI and ACI on regional meteorology and air quality; (2) added sensitivity simulations to inspect the impacts of ARI and ACI on the simulated Chinese surface $PM_{2.5}$ concentrations in winter; and (3) compared the computational performance of one-way and two-way coupled simulations using WRF-GC v2.0. We also revised the writing to improve clarity throughout and to keep the manuscript within reasonable length.

We respond to each specific comment in detail below. The referee comments are shown in red italics. Our replies are shown in black and modified text is shown in blue. The annotated page and line numbers refer to the revised copy of the manuscript.

1 Reviewer #1

General Comments

The authors developed and presented the WRF-GC model v2.0, an online two-way coupling of the Weather Research and Forecasting (WRF) meteorological model (v3.9.1.1) and the GEOS-Chem chemical model (v12.7.2). The main feature of the WRF-GC v2.0 includes aerosol-radiation Interactions (ARI) and aerosol-cloud interactions (ACI). The authors evaluated the sensitivity simulations with different combinations of ARI and ACI over

East Asia during January 2015 and July 2016 using WRF-GC v2.0 The manuscript is well structured. The objective and methodology described in the manuscript are clear. However, some revisions on the results (chapter 4 and 5) are required prior to the recommendation. Please refer to the major comments below.

Major comments:

R1.1 Table 1. Why did the authors conduct the sensitivity experiments with ARI and ACI only on Case Summer? If possible, please add the additional sensitivity experiments on Case Winter or one-year test.

Thanks for your suggestions. We added three new sensitivity experiments for January 2015 with different combinations of chemical feedbacks (Cases ARIw, ACIw, NO_ACRw). We compared and discussed the impacts of ARI and ACI to simulated regional meteorology and surface air quality in Section 4 and Section 5. We also added Tables 5 and 6 to summarize the performance of the different sensitivity experiments.

Table 4: Configurations of WRF-GC v2.0 experiments in this study

Experiment	Case ACRs (Case Summer)	Case ARIs	Case ACIs	Case NO_ACRs
Simulation time (UTC)	2016-06-27 00Z to 2016-07-31 00Z			
Microphysics	Morrison two-moment (Morrison et al., 2009)			
Shortwave radiation	RRTMG (Iacono et al., 2008)			
Longwave radiation	RRTMG (Iacono et al., 2008)			
Planetary boundary Layer	MYNN2 (Nakanishi and Niino, 2006)			
Land surface	Noah (Chen and Dudhia, 2001a,b)			
Surface layer	MM5 Monin-Obukhov (Jimenez et al., 2012)			
Cumulus parameterization	New Tiedtke (Tiedtke, 1989; Zhang et al., 2011; Zhang and Wang, 2017)			
Aerosol-radiation interaction	On	On	Off	Off
Aerosol-cloud interaction	On	Off	On	Off
Experiment	Case ACRw (Case Winter)	Case ARIw	Case ACIw	Case NO_ACRw
Simulation time (UTC)	2015-01-04 00Z to 2015-01-29 00Z			
Microphysics	Morrison two-moment (Morrison et al., 2009)			
Shortwave radiation	RRTMG (Iacono et al., 2008)			
Longwave radiation	RRTMG (Iacono et al., 2008)			
Planetary boundary Layer	YSU (Hong et al., 2006)			
Land surface	Noah (Chen and Dudhia, 2001a,b)			
Surface layer	MM5 Monin-Obukhov (Jimenez et al., 2012)			
Cumulus parameterization	New Tiedtke (Tiedtke, 1989; Zhang et al., 2011; Zhang and Wang, 2017)			
Aerosol-radiation interaction	On	On	Off	Off
Aerosol-cloud interaction	On	Off	On	Off

P13-14, L368-370, L378-383, Section 4.1

We next evaluate WRF-GC's performance in simulating regional meteorology and surface pollutant concentrations. We conduct two control simulations with full aerosol-cloud-radiation interactions using WRF-GC v2.0, one during January 2015 (Case ACRw) and one during July 2016 (Case ACRs). Table 4 summarizes the setup of our simulations.

We further conduct sensitivity simulations over China for January 2015 and July 2016 with different combinations of ARI and ACI to investigate the impacts of chemical feedbacks on simulated meteorology and air quality (Table 4). The setup of these sensitivity simulations are identical to the control cases, except ARI and ACI are configured differently in each sensitivity simulation (Table 4). In Cases NO_ACRs and NO_ACRw, both ARI and ACI are turned off, i.e., one-way WRF-GC simulations with no chemical feedbacks to meteorology. The Cases ARIs/ARIw and the Cases ACIs/ACIw simulations include either ARI or ACI, respectively.

P16, L473-476, Section 4.4

Figures 6a and 6b show the observed and simulated (Case ACRw) average LCODs during January 8 to 28, 2015. The model reproduces the spatial distribution of LCODs observed by VIIRS over China, including in particular the high LCODs over Southern China. However, the simulated LCOD is considerably lower than the VIIRS LCOD observations elsewhere in the domain.

P17, L486-496, Section 4.5

Figures 9a and 9b compare the mean SWDOWN observed by CERES and that simulated by WRF-GC (Case ACRw) during January 8 to 28, 2015. The spatial distribution of the simulated wintertime SWDOWN also agrees well with the satellite observations, with a spatial correlation coefficient of 0.93 over the domain. The domain-average observed and simulated SWDOWN are 111 ± 45 W m^{-2} and 140 ± 55 W m^{-2}, respectively (model NMB = 25.9%). The overestimation of wintertime SWDOWN is over the Sichuan Basin, the Tibetan Plateau and the

Southern China, possibly related to the model's underestimation of AOD and LCOD over these areas in winter.

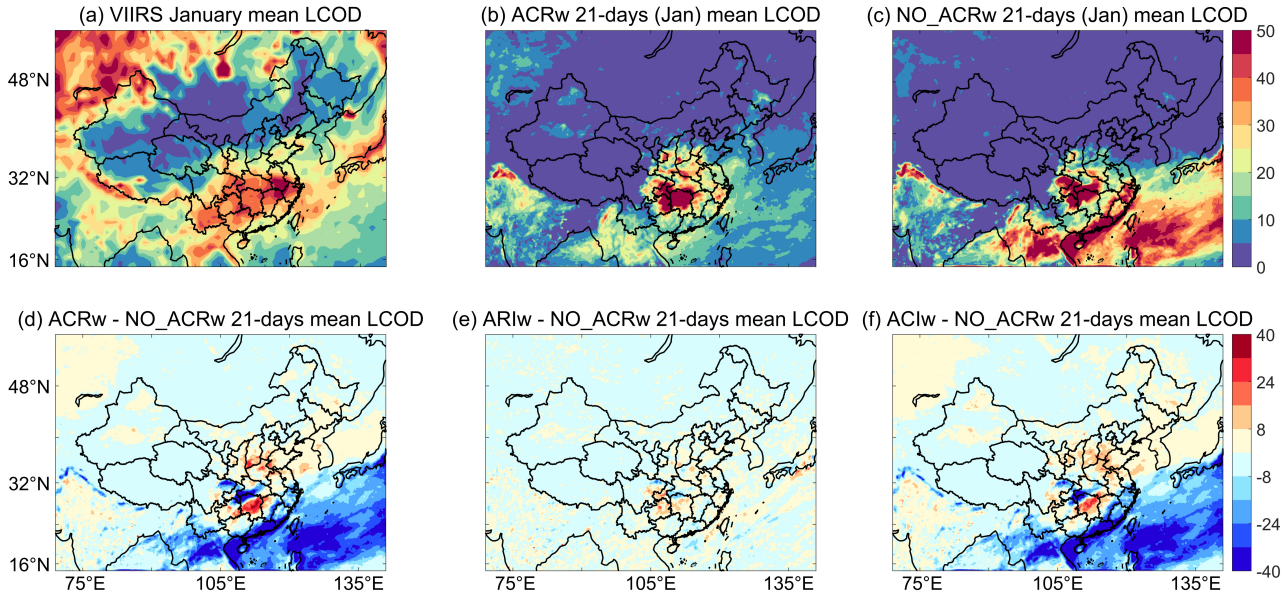

Figure 6: Mean LCOD from (a) VIIRS observations (monthly mean in during January 2015), (b) the Case ACRw simulation, and (c) the Case NO_ACRs simulation during January 8 to 28, 2015. Also shown are the differences in simulated LCOD between (d) Case ACRw and Case NO_ACRw, (e) Case ARIw and Case NO_ACRw, and (f) Case ACIw and Case NO_ACRw during January 8 to 28, 2015.

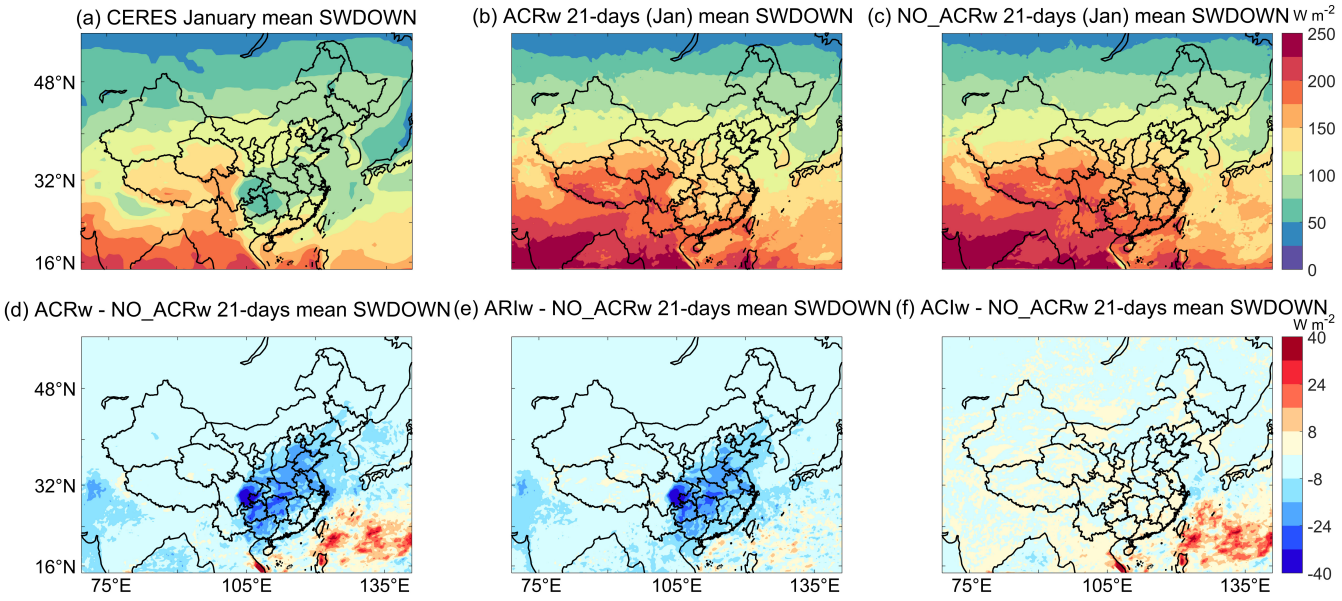

Figure 9: Mean surface downward shortwave radiation (SWDOWN) from (a) CERES observations (monthly mean in January), (b) the Case ACRw simulation, and (c) the Case NO_ACRw simulation during January 8 to 28, 2015. Also shown are the differences in simulated mean SWDOWN between (d) Case ACRw and Case NO_ACRw, (e) Case ARIw and Case NO_ACRw, and (f) Case ACIw and Case NO_ACRw during January 8 to 28, 2015.

P17, L497-502, Section 4.5

Figure 10a and Figure 11a show the good agreement between the simulated and observed surface air temperature over China during July 2016 (Case ACRs) and during January 8 to 28, 2015 (Case ACRw), respectively. The spatial correlation coefficients between the observed and simulated surface air temperature are 0.92 (Case ACRs) and 0.93 (Case ACRw), respectively. During July 2016, the simulated and observed surface air temperature averaged over all sites are 23.7 ± 5.9 °C and 24.6 ± 5.0 °C, respectively (NMB of -3.7%). During January 8 to 28, 2015, the simulated surface air temperature averaged over all sites is 7.2 ± 6.7 °C, with a model NMB of -13.3 % relative to the observations.

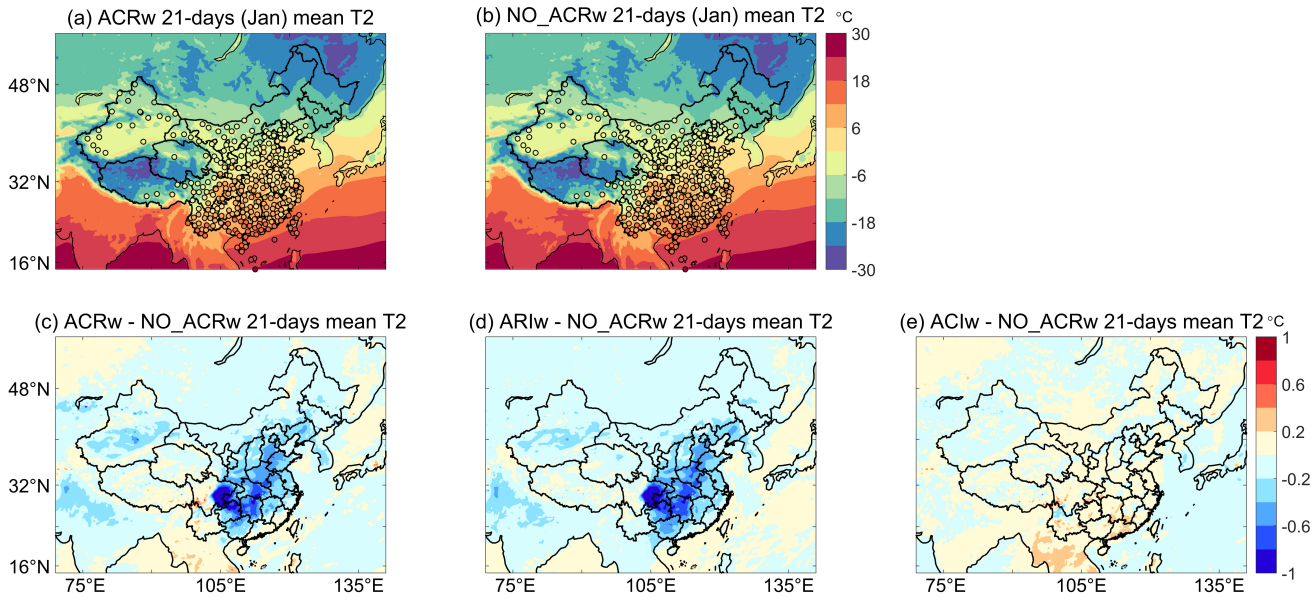

Figure 11: Comparison of the observed (filled symbols) and simulated (filled contours) mean surface air temperature from (a) Case ACRw and (b) Case NO_ACRw during January 8 to 28, 2015. Also shown are the differences in simulated mean surface air temperature between (c) Case ACRw and Case NO_ACRw, (d) Case ARIw and Case NO_ACRw, and (e) Case ACIw and Case NO_ACRw during January 8 to 28, 2015.

P18, L536-537, Section 5.1

Figures 5 and 6 show the impacts of ARI and ACI on the simulated LCOD in July 2016 and in January 2015, respectively.

P18, L539-544, Section 5.1

In particular, we find that the inclusion of ACI greatly reduces the simulated LCOD in both seasons; the inclusion of ACI corrects the high-biased LCODs simulated by Cases NO_ACRs and NO_ACRw, particularly over Central and Southern China, around Japan and Korea, and along the southern slopes of the Himalayas. In Cases ACRs and ACRw, the simulated monthly mean CCN concentrations (at 0.1 % supersaturation) averaged from the cloud bottom to cloud top are 150 cm^{-3} and 58 cm^{-3}, respectively. However, when ACI is turned off, WRF-GC uses a constant, high CCN activation rate (250 cm^{-3} per time step), leading to overestimation of cloud droplet numbers (effectively around 250 cm^{-3}) and thus LCOD.

P18, L545, Section 5.1

Figure 8 and 9 show the impacts of ARI and ACI on the simulated SWDOWN in July 2016 and January 2015, respectively.

P18, L552-561, Section 5.1

In January, the inclusion of ARI reduces the simulated SWDOWN over Eastern China by 8 to 40 W m^{-2}, while the inclusion of ACI does not significantly affect the simulated SWDOWN.

Figures 10 and 11 compare the simulated mean surface air temperature from the sensitivity experiments during July 2016 and January 2015, respectively.

In January, the impacts of ARI on surface air temperature are much stronger than the impacts of ACI. Upon closer inspection, we find that the simulated responses of surface air temperature to ARI and ACI are spatially similar to the simulated responses of SWDOWN, but with some exception.

P19, L574-579, Section 5.2

Figures 14d,e,f shows the combined and individual impacts of ARI and ACI on the simulated surface $PM_{2.5}$ concentrations during January 8 to 28, 2015, relative to the simulation when both ARI and ACI are turned off. Table 6 summarizes the assessment of the simulated surface $PM_{2.5}$ concentrations against surface measurements. The inclusion of ARI significantly increases the simulated surface $PM_{2.5}$ concentrations by 6 μg m^{-3} to 15 μg m^{-3} over parts of Northern and Southern China, and the Sichuan Basin, thereby improving the agreement with surface observations (Table 6, model versus observation slope = 0.97 in Case ACRw and 0.9 in Case NO_ACRw, respectively).

Table 6: Comparison between the $PM_{2.5}$ and afternoon ozone concentrations simulated by sensitivity experiments against the surface observations during July 2016 and January 2015

$PM_{2.5}$: 388 sites over Eastern China [μg m^{-2}]			
	Mean $\pm$ stdev	R	Slope
Case ACRw	80.8 ± 32.6	0.77	0.97
Case ARIw	81.6 ± 32.6	0.77	0.97
Case ACIw	77.9 ± 30.4	0.78	0.9
Case NO_ACRw	78.8 ± 30.4	0.78	0.9
Afternoon ozone: 426 sites over Eastern China [ppbv]			
	Mean $\pm$ stdev	R	Slope
Case ACRs	64.2 ± 16.9	0.56	1.33
Case ARIs	64.7 ± 17.1	0.57	1.34
Case ACIs	65.0 ± 17.6	0.54	1.38
Case NO_ACRs	63.6 ± 17.6	0.52	1.38

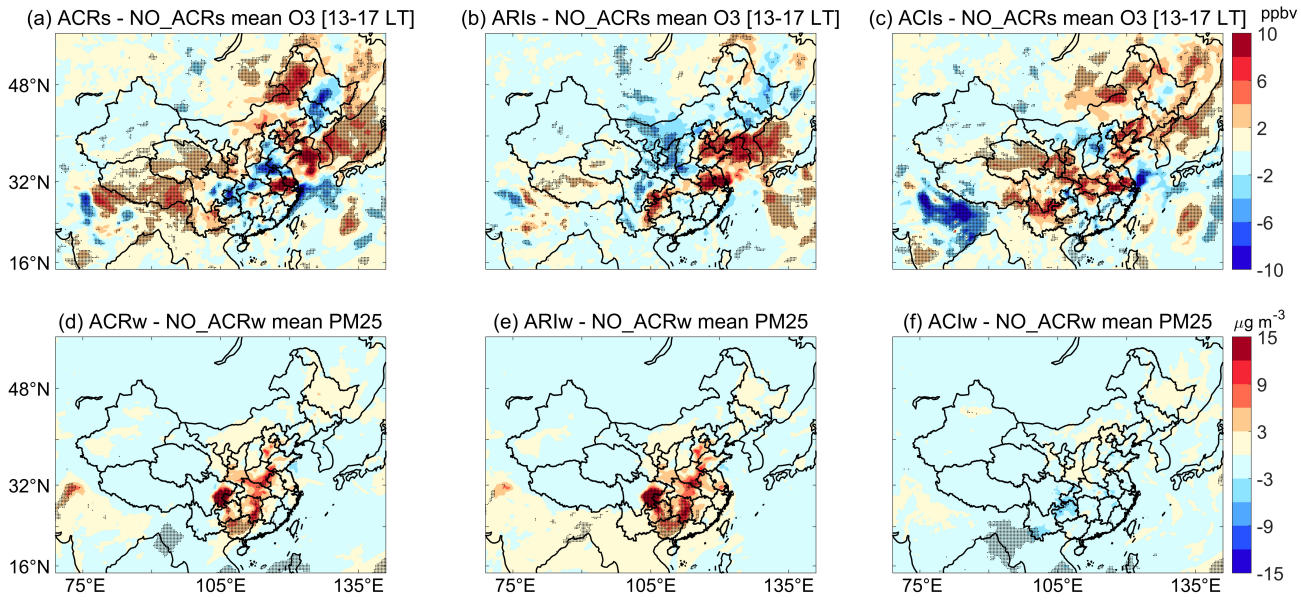

Figure 14: Differences in simulated monthly mean afternoon (13:00 to 17:00 local sun time) surface ozone concentrations during July 2016 (a) between Case ACRs and Case NO_ACRs, (b) between Case ARIs and Case NO_ACRs, and (c) between Case ACIs and Case NO_ACRs. Differences of simulated mean $PM_{2.5}$ concentrations during January 8 to 28, 2015 (d) between Case ACRw and Case NO_ACRw, (e) between Case ARIw and Case NO_ACRw , and (f) between Case ACIw and Case NO_ACRw. Stippled grids represent significant differences (two-tail t-test at 5% significance level).

R1.2 Chapter 4.3, 4.4, 4.5, 4.6 (Validation of the simulated AOD, LCOD, surface downward shortwave radiation, and air temperature). Among the sensitivity simulations with different combinations of ARI and ACI, the Case ACR (ARI and ACI are both turned on) had the best consistency with the best observed values? Author should show the model performance evaluation (MPE) in depth prior to the sensitivity experiments. I believe model sensitivity itself dose not tell many things.

Thanks you for pointing out this lack of clarity. We added Table 5 to validate the control experiments (Cases ACRs and ACRw) against observations, as well as to compare the performance of each sensitivity experiments in simulating regional meteorology. We also revised the text to describe the validation of the control experiments against observations. For all regional meteorological or air quality parameters examined in this paper, the simulations with

both ARI and ACI consistently showed best agreement with the observations.

P18, L534-544, Section 5.1

Table 5 summarized the comparison between the monthly mean meteorological variables simulated by the sensitivity experiments and the observations.

In both seasons, the simulated LCODs over Eastern China agree best with the VIIRS observations when ARI and ACI are both turned on (Cases ACRs and ACRw), compared to the sensitivity simulations when ARI or ACI, or both, are turned off (Table 5).

In Cases ACRs and ACRw, the simulated monthly mean CCN concentrations (at 0.1 % supersaturation) averaged from the cloud bottom to cloud top are 150 cm^{-3} and 58 cm^{-3}, respectively. However, when ACI is turned off, WRF-GC uses a constant, high CCN activation rate (250 cm^{-3} per time step), leading to overestimation of cloud droplet numbers (effectively around 250 cm^{-3}) and thus LCOD.

P18, L546-547, Section 5.1

Again, the simulated SWDOWN over China are most consistent with EPIC-derived and CERES observations, in terms of magnitudes and spatial correlations, when both ARI and ACI are turned on (Table 5).

P19, L552-554, Section 5.1

In January, the inclusion of ARI reduces the simulated SWDOWN over Eastern China by 8 to 40 W m^{-2}, while the inclusion of ACI does not significantly affect the simulated SWDOWN.

P19, L556-558, Section 5.1

Again, the inclusion of both ARI and ACI leads to best agreement between the observed and simulated surface air temperature in both seasons (Table 5).

Table 5: Comparison of the simulated liquid cloud optical depth (LCOD), surface downward shortwave radiation (SWDOWN), and surface temperature (T2) from sensitivity experiments against satellite and surface observations during July 2016 and January 2015

	Case ACRs	Case ARIs	Case ACIs	Case NO_ACRs	Case ACRw	Case ARIw	Case ACIw	Case NO_ACRw
LCOD over Eastern China (eastward of 100 °E) against VIIRS observations								
Mean ± stdev	13.0 ± 8.6	22.1 ± 13.0	12.5 ± 8.1	21.8 ± 12.4	9.8 ± 10.4	17.3 ± 18.7	9.6 ± 10.4	17.1 ± 18.6
R	0.64	0.65	0.60	0.62	0.48	0.34	0.46	0.33
RMSE	8.4	10.9	8.7	10.7	15.2	18.4	15.4	18.5
SWDOWN [W m^{-2}] over China against EPIC-derived observations (July) and CERES observations (January)								
Mean ± stdev	281 ± 48	274 ± 49	287 ± 49	278 ± 51	140 ± 55	139 ± 55	144 ± 57	143 ± 56
R	0.73	0.65	0.65	0.57	0.93	0.92	0.91	0.9
RMSE	33.7	40.4	37.5	43.5	36.3	35.4	41.2	40.4
T2 [°C] over China against surface measurements (215 sites in July, 150 sites in January)								
Mean ± stdev	23.7 ± 5.9	23.7 ± 6.1	23.8 ± 6.0	23.8 ± 6.0	7.2 ± 6.7	7.1 ± 6.7	7.4± 6.7	7.3 ± 6.6
R	0.92	0.93	0.92	0.92	0.93	0.93	0.93	0.93
RMSE	2.52	2.57	2.56	2.57	2.7	2.8	2.6	2.7

R1.3 Overall, this manuscript is missing interpretations of key physical/chemical processes related to ARI and ACI in the WRF-GC model v2.0. In chapter 5, there is no explanation on the impacts of ARI and ACI on the meteorological factors and air pollutants.

Thank you for pointing out this omission. We added diagnostic figures of the impacts of ARI and ACI, either individually or combined, on surface downward shortwave radiation (Figures 8 and 9), surface air temperature (Figures 10 and 11), wintertime boundary layer height (Figure 12), wintertime surface $PM_{2.5}$ and summertime afternoon surface ozone (Figure 14), and the summertime net chemical tendency of boundary-layer ozone (Figure 15). We also significantly expanded the discussion (Section 5) of the mechanisms by which ARI and ACI modulated air temperature and surface radiation, and subsequently affected the boundary layer height in winter and the ozone chemical production in summer.

P19-20, L580-587, Section 5.2

Figures 12c,d,e show the combined and individual impacts of ARI and ACI on the simulated PBLH during January 8 to 28, 2015, relative to the simulation when both ARI and ACI are turned off. We find that the simulated response of surface $PM_{2.5}$ to ARI is spatially consistent with the simulated responses of SWDOWN, surface air temperature, and PBLH to ARI. Over the Sichuan Basin and parts of Northern and Central China, the strong aerosol extinction decrease the SWDOWN and surface air temperature, resulting in lower PBLH and a possibly more stable conditions within the PBL. The shallower and more stable PBL suppresses the dispersion of air pollutants, thus increasing surface $PM_{2.5}$ concentrations. These findings are consistent with previous studies (Wang et al., 2014; Li et al., 2017; Zhang et al., 2018), although other feedback mechanisms may also play a role.

P20, L589-596, Section 5.3

Figures 14a,b,c show the combined and individual effects of the ARI and ACI on the simulated mean surface afternoon ozone concentrations in July 2016, relative to the Case NO_ACRs experiment. Overall, the inclusion of ARI and ACI in WRF-GC slightly reduces the model's positive bias in simulated surface ozone concentration (Table 6; model versus observation slope is 1.33 in Case ACRs and 1.38 in Case NO_ACRs, respectively). By including both ARI and ACI, the simulated July afternoon surface ozone concentration decrease by 2 to 10 ppbv over Henan Province, the Sichuan Basin, and parts of Northeastern China. Over the YRD area and Eastern Inner Mongolia, turning on ARI and ACI leads to increased afternoon surface ozone concentrations by up to 10 ppbv. These results are due to the spatially-varied responses of surface ozone to ARI and ACI, respectively (Figure 14).

P20, L597-612, Section 5.3

We further diagnose the net chemical mass tendency of the simulated ozone in the boundary layer over China during July 2016, to elucidate the mechanisms by which ARI and ACI affect boundary-layer ozone. The net chemical mass tendency (unit: kg s^{-1}) is the net rate of change of boundary-layer ozone mass due to chemical production and loss processes over each model grid, and its responses to ARI and ACI are shown in Figure 15. We find that the spatial responses of the net chemical mass tendency of ozone to ARI and ACI are very similar to the simulated responses of surface afternoon ozone, SWDOWN, and surface air temperature to these chemical feedbacks (Figures

8, 10, and 14). This indicates that ARI and ACI affect surface ozone mainly by modulating SWDOWN and surface air temperature, which in turn affect the emissions of biogenic isoprene and the subsequent chemical production of ozone in the boundary layer. For example, ARI lead to increased surface air temperature over the YRD area, while both ARI and ACI lead to increased SWDOWN over that area. These meteorological responses lead to enhanced local biogenic isoprene emissions and increased surface ozone. Over the Beijing-Tianjin-Hebei (BTH) area of China, where summertime ozone pollution is most severe (Lu et al., 2018), the effects of ARI and ACI are complex. ARI and ACI both reduce the local SWDOWN (Figures 8e,f), while ARI increases surface air temperature over southern BTH and ACI suppresses surface air temperature over the entire BTH (Figures 10d,e). The combined effect of chemical feedbacks is to increase surface ozone over northern BTH, while decreasing surface ozone over southern BTH. ARI and ACI may also modulate other meteorological variable to affect surface ozone, and such possibilities warrants further investigation.

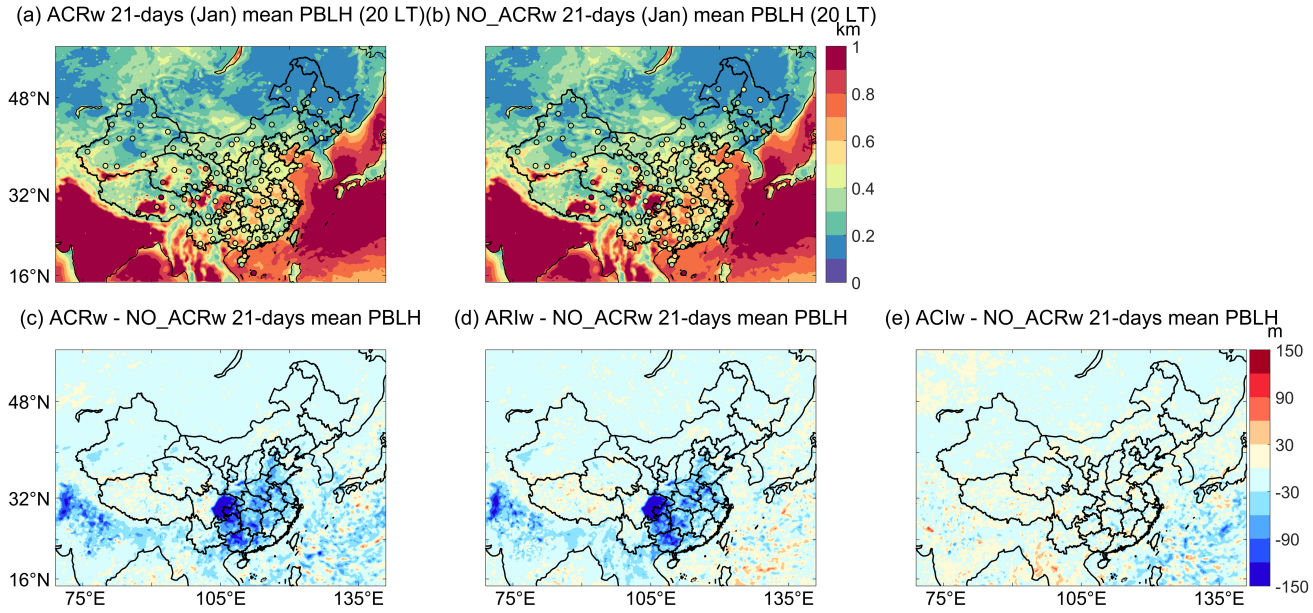

Figure 12: Comparison of the observed (filled symbols) and simulated (filled contours) mean planetary boundary layer heights (PBLH) at 20:00 local time (12:00 UTC) from (a) Case ACRw and (b) Case NO_ACRw during January 8 to 28, 2015. Also shown are the differences in simulated PBLH at 20:00 local time (12:00 UTC) between (c) Case ACRw and Case NO_ACRw, (d) Case ARIw and Case NO_ACRw, and (e) Case ACIw and Case NO_ACRw during January 8 to 28, 2015.

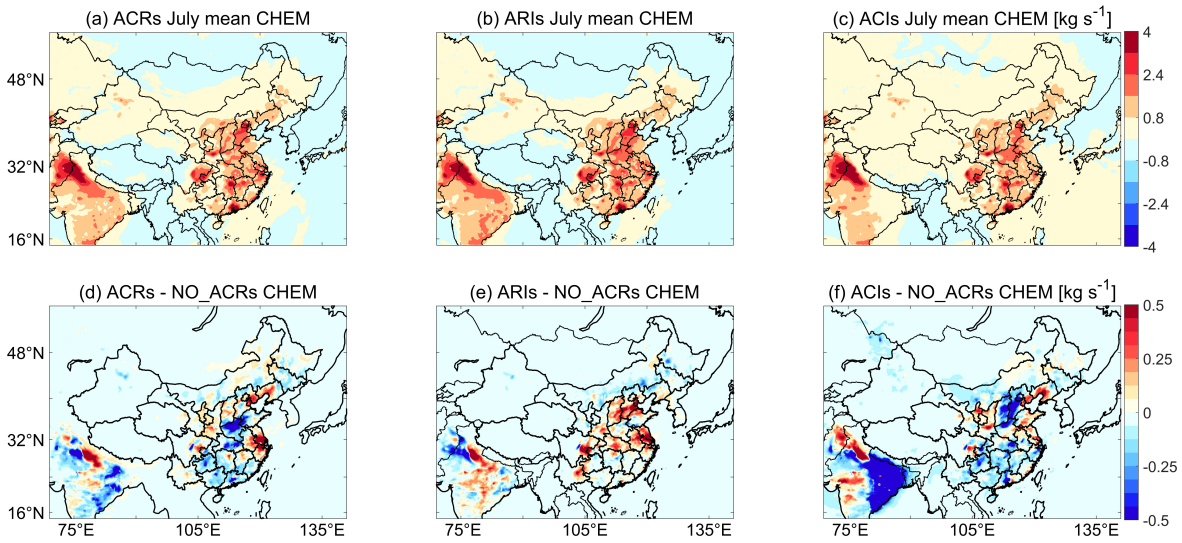

Figure 15: Mean simulated chemical mass tendency (unit: kg s^{-1}) for afternoon boundary-layer ozone from (a) Case ACRs, (b) Case ARIs, and (c) Case ACIs during July 2016. Also shown are the differences in simulated chemical mass tendencies for afternoon boundary-layer ozone between (d) Case ACRs and Case NO_ACRs, (e) Case ARIs and Case NO_ACRs, and (f) Case ACIs and Case the NO_ACRs in July 2016.

R1.4 Considerations of ARI and ACI in the WRF-GC v2.0 can alter a variety of meteorological factors in addition to the surface temperature and shortwave radiation as mentioned in the manuscript. Authors should add the analysis for the impacts of ARI and ACI on other meteorological factors, such as planetary boundary layer, relative humidity, and so on.

Thanks for your suggestions. We diagnosed the response of wintertime surface $PM_{2.5}$ to ARI through modulation of surface air temperature and PBLH (Section 5.2), as well as the response of summertime surface afternoon ozone to through modulation of radiation and temperature (Section 5.3). We also pointed out that ARI and ACI may also affect other meteorological variables to alter air quality, and that such possibilities may be further investigated using WRF-GC.

P19, L566-572, Section 5.1

The simulated PBLH are also chemically-sensitive, especially in winter. Figure 12 compare the simulated mean

PBLH at 20:00 local time (12:00 UTC) from the sensitivity experiments during January 8 to 28, 2015. The simulated PBLH from Case ACRw (462 ± 176 m) better agrees with the observations (448 ± 129 m), compared to the simulated PBLH from Case NO_ACRw (491 ± 195 m). We find that the inclusion of ARI reduces the simulated PBLH throughout Eastern China, particularly over the Sichuan Basin. This response is consistent with previous studies that showed the strong aerosol extinction in winter has a positive feedback to surface $PM_{2.5}$ concentration via the compression of PBLH (Li et al., 2017; Zhang et al., 2018; Miao and Liu, 2019).

P20, L580-587, Section 5.2

Figures 12c,d,e show the combined and individual impacts of ARI and ACI on the simulated PBLH during January 8 to 28, 2015, relative to the simulation when both ARI and ACI are turned off. We find that the simulated response of surface $PM_{2.5}$ to ARI is spatially consistent with the simulated responses of SWDOWN, surface air temperature, and PBLH to ARI. Over the Sichuan Basin and parts of Northern and Central China, the strong aerosol extinction decrease the SWDOWN and surface air temperature, resulting in lower PBLH and a possibly more stable conditions within the PBL. The shallower and more stable PBL suppresses the dispersion of air pollutants, thus increasing surface $PM_{2.5}$ concentrations. These findings are consistent with previous studies (Wang et al., 2014; Li et al., 2017; Zhang et al., 2018), although other feedback mechanisms may also play a role.

R1.5 The results and discussion are too general. What would be benefits of the on-line model applications? If the purpose of the model update or development is to simulate the regional-scale interaction between meteorology and air pollutants, the modeling capability should be thoroughly validated as if other regional photochemical models conventionally do. Model performance evaluations against the surface measurements of the criteria air pollutants including PM2.5 and O3 are recommended. After that, model sensitivities with or without the ARI and ACI can show the results of the interactions.

Thanks for your suggestions. We added Tables 5 and 6 (shown in R1.1) to validate the control experiments (Cases

ACRs and ACRw) against observations, as well as to compare the performance of each sensitivity experiments in simulating regional meteorology and chemistry. We also revised the text to describe the validation of the control experiments against observations. We compared and discussed the impacts of ARI and ACI to simulated regional meteorology and surface air quality in Section 5. We also added Tables 5 and 6 to summarize the performance of the different sensitivity experiments. The validation for meteorological variables is shown in R1.2.

P19, L575-579, Section 5.2

Table 6 summarizes the assessment of the simulated surface $PM_{2.5}$ concentrations against surface measurements. The inclusion of ARI significantly increases the simulated surface $PM_{2.5}$ concentrations by 6 μg m^{-3} to 15 μg m^{-3} over parts of Northern and Southern China, and the Sichuan Basin, thereby improving the agreement with surface observations (Table 6, model versus observation slope = 0.97 in Case ACRw and 0.9 in Case NO_ACRw, respectively).

P20, L590-594, Section 5.3

Overall, the inclusion of ARI and ACI in WRF-GC slightly reduces the model's positive bias in simulated surface ozone concentration (Table 6; model versus observation slope is 1.33 in Case ACRs and 1.38 in Case NO_ACRs, respectively). By including both ARI and ACI, the simulated July afternoon surface ozone concentration decrease by 2 to 10 ppbv over Henan Province, the Sichuan Basin, and parts of Northeastern China.

R1.6 Specific comments and typos:

Line 407: Add a comma before the "2015" in 'during January 8 to 28, 2015'.

Line 414 : at 550 nm in July

Line 474 : Please revise the subscripts. (for example, $PM_{2.5}$ à PM2.5)

Corrected. Thank you for pointing out the mistakes.

P15, L430, Section 4.3

Figure 3a and 3c compare the AOD at 550 nm wavelength over East Asia as observed by VIIRS and as simulated by WRF-GC (Case ACRw) during January 8 to 28, 2015.

Figures 3b and 3d compare the observed and simulated (Case ACRs) mean AOD at 550 nm during July 2016.

P18, L518-519, Section 4.6

WRF-GC successfully captures the high $PM_{2.5}$ in Central China and over the Sichuan Basin but underestimates the $PM_{2.5}$ concentrations over the NCP.

2 Reviewer #2

This is a well-organized and written manuscript. Built on their previous work published on GMD, the authors further developed WRF-GC to enable feedbacks of aerosol-cloud and aerosol-radiation interactions. The latest model edition also supports the nest-domain capability. Both GEOS-Chem and WRF models are actively developed and embrace a large user base worldwide. Coupling them together is a great contribution to the modeling community. This reviewer recommends publication after minor revisions listed below.

R2.1 In the text, spell out all the acronyms, e.g., WRF-GC, CMAQ, COSMO, SSA, and many more, when they first appear.

Thank you for pointing out the omissions. We now spell out all acronyms when they first appear. For example:

P2, L39-44, Introduction

A number of two-way models are coupled using the online-access approach, including for example the online WRF-Community Multiscale Air Quality model (WRF-CMAQ) (Byun and Schere, 2006; Wong et al., 2012; Yu et al., 2014), the Global Environmental Multiscale-Air Quality model (GEM-AQ) (Kaminski et al., 2008), the Consortium for Small-Scale Modelling-Multiscale Chemistry Aerosol Transport model (COSMO-MUSCAT) (Wolke et al., 2004; Renner and Wolke, 2010), and the Integrated Forecast System-Model for Ozone And Related Tracers model (IFS-MOZART) (Flemming et al., 2009).

P7, L181-182, Section 2.2.2

In WRF, two shortwave radiation schemes are coupled to prognostic aerosol information: the Rapid Radiative Transfer Model for Global Circulation Model (RRTMG) shortwave radiation scheme (Iacono et al., 2008) and the Goddard shortwave radiation scheme (Chou and Suarez, 1994).

P7, L193, Section 2.2.2

The AOD is interpolated or extrapolated using the Ångström exponent method (Eck et al., 1999), while the single scattering albedo (SSA) and the asymmetry factor are linearly interpolated.

P12, L331-332, Section 3.5

The emission module of GEOS-Chem, the Harmonized Emissions Component (HEMCO), has also been updated to fully objectify its memory space (Keller et al., 2014; Lin et al., 2021).

R2.2 Line 45, replace "advances" with "advancement".

Changed as suggested. Thank you.

P2, L45-47, Introduction

As such, these stand-alone CTMs may be independently developed by a wider atmospheric chemistry community, and the resulting CTM advancement may be quickly incorporated into the coupled model via the online-access structure (Yu et al., 2014).

R2.3 Table 1, DST4 should be "dust bin 4".

Corrected as suggested. Thank you.

P46, Table 1

Table 1: Aerosol types in WRF-GC and their prescribed properties and size distributions

Name	**Species**	**Molecular weight** ($g \cdot mol^{-1}$)	**Density** ($g \cdot cm^{-3}$)	**Hygroscopicity** (unitless)	**Log-normal distribution** (Geometric mean dry diameter, μm)	**Log-normal distribution** (Geometric standard deviation, unitless)
SO4	sulfate	96	1.7	0.5	0.14	1.6
NIT	nitrate	62	1.8	0.5	0.14	1.6
NH4	ammonium	18	1.8	0.5	0.14	1.6
OCPI	hydrophilic primary OC	12	1.3	0.2	0.14	1.6
OCPO	hydrophobic primary OC	12	1.3	0.2	0.14	1.6
BCPI	hydrophilic BC	12	1.8	1.00E-06	0.04	1.6
BCPO	hydrophobic BC	12	1.8	1.00E-06	0.04	1.6
SALA	accumulation-mode sea salt (radius 0.1 - 0.5 μm)	31.4	2.2	1.16	0.18	1.5
SALC	coarse-mode sea salt (radius 0.5 - 4.0 μm)	31.4	2.2	1.16	0.8	1.8
DST1	dust bin 1 (radius 0.1 - 1.0 μm)	29	2.5	0.14	–	–
DST2	dust bin 2 (radius 1.0 - 1.8 μm)	29	2.65	0.14	–	–
DST3	dust bin 3 (radius 1.8 - 3.0 μm)	29	2.65	0.14	–	–
DST4	dust bin 4 (radius 3.0 - 6.0 μm)	29	2.65	0.14	–	–
SOAS	SOA (simple)	150	1.5	0.14	0.14	1.6

R2.4 Line 389, change "over than 440 nm" to "over 440 nm".

Corrected as suggested. Thank you.

P14, L410-412, Section 4.2.2

Holben et al. (1998) showed that the uncertainty of AERONET AOD under cloud-free condition was less than $\pm$ 0.01 for wavelengths over 440 nm.

R2.5 Line 400, why not include all the monitoring sites within a grid cell for model evaluation?

Thank you for the suggestion. We now calculate the averaged concentrations of $PM_{2.5}$ and ozone of all sites within a model grid cell for comparison with model simulations.We update the Figure 13 and validations as follows:

P15, L419-421, Section 4.2.3

For comparison between observations and model results, we calculate the average $PM_{2.5}$ and ozone measurements in a WRF-GC grid. In all, we compare model results to summertime ozone observations at 562 sites and wintertime $PM_{2.5}$ at 513 sites, respectively.

P18, L515-529, Section 4.6

WRF-GC reproduces the observed spatial distributions of $PM_{2.5}$ over Eastern China (eastward of 108° E); the spatial correlation between the observed and simulated $PM_{2.5}$ concentrations is 0.77. The simulated mean $PM_{2.5}$ concentration over Eastern China (80.8 ± 32.6 μg m^{-3}) is 9.3% lower than the observations (89.1 ± 31 μg m^{-3}).

WRF-GC also underestimates $PM_{2.5}$ over Western China, likely reflecting a low-bias in the model dust, also seen in the simulated AODs. WRF-GC also reproduces the temporal variation of hourly $PM_{2.5}$ during January 8 to 28, 2015. The temporal correlation coefficient between the observed and simulated hourly $PM_{2.5}$ averaged over all Chinese sites is 0.77.

WRF-GC reproduces the higher surface ozone concentrations over Northern and Central China, the relatively lower ozone concentrations near the South China coast, and the ozone hotspots over the megacity clusters (Beijing-Tianjin-Hebin, Yantze River Delta, and the Pearl River Delta). However, the surface afternoon ozone concentrations simulated by WRF-GC (64 ± 17 ppbv) is high-biased compared to the observations (51 ± 13 ppbv). The normalized mean bias of the simulation is 25.6%. The overestimation of surface ozone concentrations is most severe over Henan and Shanxi provinces in Northern China. The temporal correlation coefficient between the observed and simulated hourly afternoon ozone concentrations averaged over all sites is 0.67.

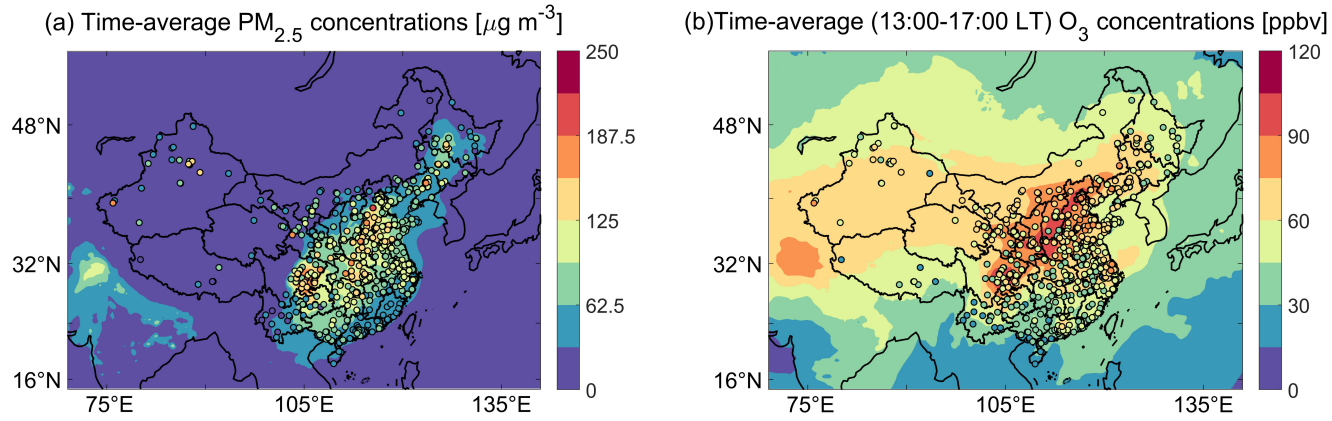

Figure 13: (a) Mean observed (symbols) and simulated (Case ACRw, filled contours) $PM_{2.5}$ concentrations during January 8 to 28, 2015; (b) mean observed (symbols) and simulated (Case ACRs, filled contours) afternoon surface ozone concentrations (13:00 to 17:00 local time) during July 2016.

R2.6 Figure 3: it appears that WRF-GC severely underestimates monthly AOD across most of the domain in comparison with the VIIRS observations. What are the possible reasons? Is it mainly due to emissions, or meteorology (e.g., humidity)? A little in-depth analysis may provide useful information for both model improvement and satellite retrieval.

Thanks for pointing out this issue. Underestimation of satellite-based AOD observations by regional models is not uncommon (Gao et al., 2014; Gan et al., 2015; Xing et al., 2015; Zhang et al., 2016). Detailed investigation and remediation of the cause are certainly important but beyond the scope of the current manuscript. We expanded the text to raise three possible reasons based on previous studies: (1) incorrect assumption about the mixing state of aerosols in the model, (2) underestimation of aerosols in the model, and (3) high-bias in the satellite AOD products. We will explore the causes for the biases of AOD in a future work. We revised the manuscript as follows:

P16, L453-463, Section 4.3

Previous comparisons of AODs simulated by regional models against satellite observations also often found spatial consistency but significant low biases in the models (Gao et al., 2014; Gan et al., 2015; Xing et al., 2015;

Zhang et al., 2016). Curci et al. (2015) showed that the uncertainties for the model AODs are associated with the assumed mixing state, refractive indices, and hygroscopicity of aerosols. In particular, assumptions of the aerosol mixing state can lead to 30% to 35% uncertainty on the simulated AOD (Fassi-Fihri et al., 1997; Curci et al., 2015). In addition, the WRF-GC model may have underestimated the abundance of aerosols over China, as indicated by the slight underestimation of surface $PM_{2.5}$ concentrations shown below (Section 4.6). On the other hand, several studies showed that the regional distributions of AOD observed by VIIRS and MODIS are consistent with the AERONET measurements, but both VIIRS and MODIS observations are high-biased compared to AERONET observations over Asia (Wang et al., 2020). This high-bias in the satellite-observed AOD may partially account for the discrepancy between the simulated and satellite AODs. The cause of the discrepancy between observed and simulated AOD should be further investigated in future studies.

R2.7 Figure 4: why not converting the modeled AOD to the one at the observed wavelength for an apple-to-apple comparison?

Thank you for the suggestion. We now interpolate the simulated spectral AODs at 400 nm, 600 nm, and 999 nm to the observed spectral AODs at 500 nm, 675 nm, and 1020 nm based on the Ångström exponent method (Eck et al., 1999). This revision does not have a large impact on the temporal correlation coefficients between the simulated and observed spectral AODs. We updated the Figure 4 and revised the text as follows:

P15, L445-450, Section 4.3

At each site, we interpolate the simulated spectral AODs at 400 nm, 600 nm, and 999 nm to the AERONET observation wavelengths of 500 nm, 675 nm, and 1020 nm, respectively, using the Ångström exponent method (Eck et al., 1999).

The temporal correlation coefficients between the observed and simulated AODs at all sites and wavelengths range between 0.55 and 0.86, except for the correlation coefficient between the observed and simulated 500 nm

AOD in Beijing (0.44).

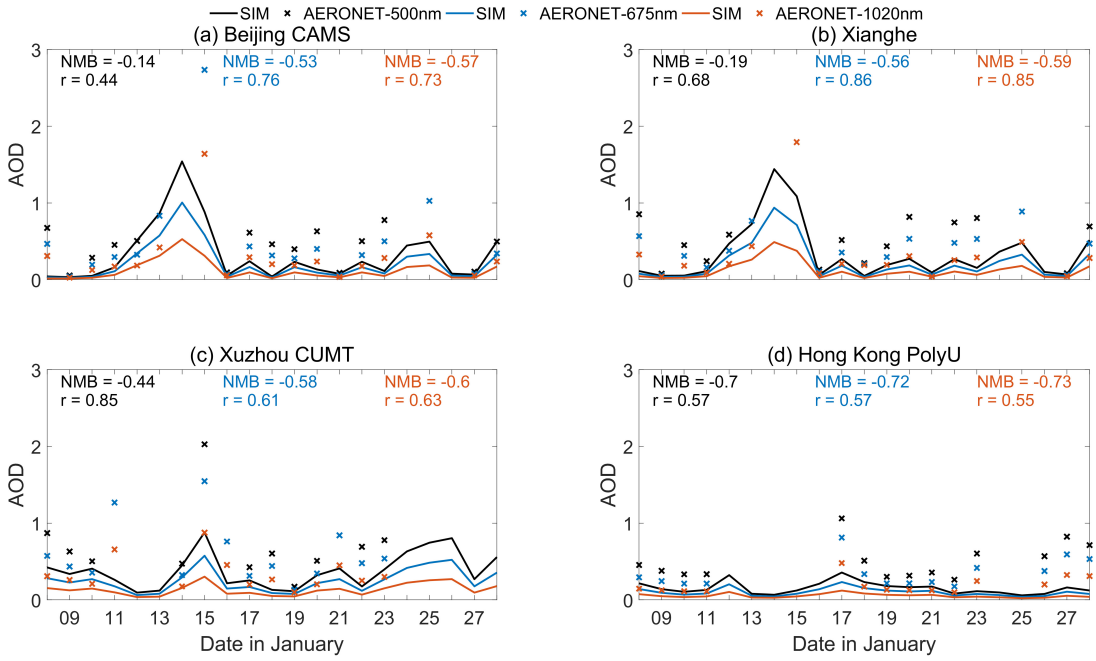

Figure 4: Comparison of simulated daily AOD (Case ACRw) against the AERONET daily AOD observations at 500 nm, 675 nm and 1020 nm at 4 sites during January 08 to January 28, 2015: (a) Beijing, (b) Xianghe, (c) Xuzhou, and (d) Hong Kong. Also shown are the normalized mean biases (NMBs) and the temporal correlation coefficients (r) between the simulated and observed spectral AODs.

R2.8 Line 451, add "cloud" after "stratocumulus or stratus".

R2.9 Line 474, change "2.5" in PM2.5 from superscript to subscript.

R2.10 Line 550, change "WRF-GC'se" to "WRF-GC's".

Corrected. Thank you for pointing out these mistakes.

P16, L477-479, Section 4.4

Satellite retrievals of cloud effective radii often show large biases, except over areas dominated by liquid stratocumulus or stratus cloud (Yan et al., 2015; Witte et al., 2018).

P18, L517-519, Section 4.6

WRF-GC successfully captures the high $PM_{2.5}$ in Central China and over the Sichuan Basin but underestimates the $PM_{2.5}$ concentrations over the NCP.

P21, L624-626, Section 6

We develop WRF-GC's nested-domain capability by improving the State Management Module and the memory-management in GEOS-Chem (implemented as of GEOS-Chem version 12.4.0).

R2.11 27 km resolution has been applied in the study for model evaluation. This resolution is too coarse to resolve cloud processes to which the ACI is important. Some discussion may be necessary to clarify this.

Thanks for pointing out the issue. Our simulations are conducted at a typical meso-scale resolution (27 km), with the cumulus parameterization (new Tiedtke) and the cloud microphysical scheme (Morrison two-moment) both turned on. Most meso-scale simulations of ACI are configure this way and thus consider only the feedback of aerosols to large-scale microphysics but do not explicity simulate the impacts of aerosol of sub-grid convective clouds (e.g., Wu et al. (2011); Zhao et al. (2017)). Wu et al. (2011) previously compared model simulations at 36-km resolution (with aerosol-sensitive large-scale microphysics and aerosol-insensitive cumulus parameterization) and at 4-km resolution (with only aerosol-sensitive large-scale microphysics). They found that the simulated sensitivity of clouds and precipitation to aerosols are similar in the meso-scale (36-km) and cloud-resolving (4-km) simulations. We revised the manuscript to clarify this.

P6, L175-180, Section 2.2.2

Most meso-scale simulations of ACI consider only the feedback of aerosols to large-scale microphysics but do not explicitly simulate the impacts of aerosol on sub-grid convective clouds (e.g., Wu et al. (2011); Zhao et al. (2017)). Also, most of the cumulus parameterization schemes in the standard WRF model (v3.9.1.1) do not respond explicitly to prognostic aerosol information. The only exception is the Grell-Freitas Ensemble scheme (Grell and Freitas, 2014), which parameterizes the conversion of cloud water to rain water as a function of prognostic cloud

condensation nuclei (CCN) number. The Grell-Freitas Ensemble scheme will be supported in a future version of WRF-GC.

R2.12 The ARI and ACI have been specifically linked to RRTMG scheme and Morrison two-moment microphysics scheme, respectively, in the application. Have the authors considered a more generalized method so that they can easily link to other radiation and microphysics schemes available to WRF?

Thanks for pointing out the lack of clarity. Our treatment of prognostic aerosol information in the WRF-GC Coupler for ARI and ACI calculations are already abstracted and generalized. These treatments in the WRF-GC Coupler can be easily applied to any other radiative and microphysical schemes that consider prognostic aerosol information. However, currently in the WRF model, only a few radiative and microphysical schemes can ingest prognostic aerosol information. All of these schemes (RRTMG shortwave and longwave, Goddard shortwave, Morrison two-moment microphysics, and Lin et al. microphysics) are supported by WRF-GC. We revised the text to clarify.

P6, L172-175, Section 2.2.2

Only a few radiative transfer and microphysics schemes in WRF are currently coupled to prognostic aerosol information, and WRF-GC v2.0 supports these existing schemes. However, our treatments of aerosol information in the two-way WRF-GC Coupler are abstracted and generalized, such that the Coupler may be extended to support other radiative and microphysical schemes in WRF in the future.

R2.13 Has WRF-GC already been included in the community WRF release? Or will it be included in the standard WRF release in the near future?

Thank you for pointing out the lack of clarity. WRF-GC, including its parent models and the Coupler (v2.0), is open-source and freely accessible from GitHub. WRF-GC has not been included in the standard WRF release, mainly

because the GEOS-Chem model is independent of WRF and is separately released. We revise the *Code availability* section to more clearly describe how to access the WRF-GC (v2.0) code.

P21, L641, Code availability

WRF-GC is free and open-source (`http://wrf.geos-chem.org`). The WRF-GC v2.0 Coupler can be downloaded from Github (`https://github.com/jimmielin/wrf-gc-release`, last accessed: May 9, 2021). The two parent models, WRF and GEOS-Chem, are also open-source and can be obtained from their developers at `https://github.com/wrf-model/WRF` (last accessed: May 9, 2021) and `http://www.geos-chem.org` (last accessed: May 9, 2021), respectively. The version of WRF-GC (v2.0) described in this paper supports WRF v3.9.1.1 and GEOS-Chem v12.7.2 and is permanently archived at `https://github.com/jimmielin/wrf-gc-pt2-paper-code-nested` (last accessed: December 27, 2020) (DOI: 10.5281/zenodo.4395258). The WRF-GC code used for the simulations described in Sections 4 and 5 is permanently archived at `https://github.com/jimmielin/wrf-gc-pt2-paper-code` (last accessed: December 19, 2020) (DOI: 10.5281/zenodo.4362624).

3 Reviewer #3

The paper presents a new online two-way coupled model WRF-GC v2.0 based on WRF meteorological model coupled with the GEOS-Chem chemical model including aerosol-radiation interactions (ARI) and aerosol-cloud interactions (ACI) based on bulk aerosol mass and composition, and nesting capability for high-resolution simulations. The authors also analyze chemical feedbacks to meteorology considering ARI and ACI mechanisms.

The paper is interesting and can be suitable for publication, but several comments need to be improved and clarified.

R3.1 The coupling structure modular, which allows the two parent models to be run off-line or online. This is definitely an advantage. However, it is difficult to classify this model as online-integrated coupled model. According to the definitions (Baklanov et al., 2014) it is still online-access coupling model, like WFR-CMAQ, because the equations of the meteo and chemical transport parts are solved separately, not on the same grid, not simultaneously in each grid-cell and not on each time step (at least it is not clear from the model description). So, in such way of coupling it is difficult to guarantee the consistency and mass-conservation. Besides, most probably the convection numerical schemes are different and not consistent in WRF and GEOS-Chem models.

Thank you for pointing out the lack of clarity in our original text. Actually, in the WRF-GC model, grid-scale advections of meteorological variables and chemical constituents are calculated with the same transport scheme; they are both performed by WRF model, on the same grid and at the same time. This is because the GEOS-Chem model is structured into modular units of atmospheric columns (Long et al., 2015; Eastham et al., 2018; Lin et al., 2020), which separates the calculation of grid-scale advection of chemical species from other chemical processes. When coupled to the dynamical models, such as the case in WRF-GC, the GEOS-Chem column model only performs convective transport, dry deposition, wet scavenging, emission, boundary layer mixing, and chemistry calculations within the vertical column. These processes are grid-independent in horizontal direction. In addition, in WRF-GC the horizontal resolution and location of GEOS-Chem vertical columns are managed by WRF, such that the meteorological and

chemical processes are solved on the same horizontal grid through operator-splitting (Baklanov et al., 2014). This treatment is exactly the same as that in the WRF-Chem model (Lin et al., 2020). Therefore, the WRF-GC model maintains mass-conservation and consistency for advection of meteorological variables and chemical species.

It is true that the convective mixing and PBL mixing schemes are not consistent in WRF and GEOS-Chem. The sub-grid vertical transports of chemical species, including convective transport (Allen et al., 1996; Wu et al., 2007) and boundary layer mixing (Lin and McElroy, 2010) are performed by GEOS-Chem and driven by WRF-simulated meteorological variables. More research is needed to investigate the impacts of this discrepancy on the two-way coupled WRF-GC model.

We revised the manuscript to more precisely describe the model framework of WRF-GC:

P4, L89-98, Section 2.1

A WRF-GC simulation is initialized and managed by WRF, which sets the global clock, dynamical and chemical time steps, domain, horizontal resolution, vertical coordinates, as well as initial/boundary conditions. In particular, the 3-D grid system is determined by WRF and is fully adopted by the GEOS-Chem chemical module in units of atmospheric columns. At each dynamical time step, WRF performs dynamical and physical calculations. WRF calculates the grid-scale advection of meteorological variables and chemical species using the same transport scheme (Wicker and Skamarock, 2002), on the same grid system, and at the same time steps, ensuring mass-conservation of the chemical species. At each chemical time step, the meteorological and chemical information is passed from WRF to GEOS-Chem through the WRF-GC Coupler. Then, the GEOS-Chem column model is called to perform convective mixing, dry deposition, emissions, planetary boundary-layer mixing, gas and aerosol chemistry, and wet scavenging (except advection), in this order, within each atmospheric column at WRF-specified horizontal locations (Lin et al., 2020).

R3.2 From other side, the model uses a coupler for data transfer from one model to other. Transfer of 3D data on each time step for each grid-cell will take a lot of time, that makes the modelling system substantially slower

in comparison with the fully online integrating approach. For example, ECMWF demonstrated that when they switched from the online-access version IFS-MOZART to the online integrated C-IFS (Huijnen et al., 2010), the modeling system became much faster.

So, it would be important to demonstrate the consistency tests and the effectiveness of the suggested way of the coupling.

Thank you for pointing this out. We added Section 3.6 to diagnose the computational performance of WRF-GC v2.0. We found that the increase in walll time in the two-way simulations relative to the one-way simulation is only slight (< 12%):

P13, L346-354, Section 3.6

We conduct two-day (June 27 to 29, 2019) simulations using the WRF-GC (v2.0) model and the GEOS-Chem Classic nested-grid model (v12.7.2), to compare their computational performance. Simulations with both models are configured with 245×181 atmospheric columns over China. The WRF-GC simulations have 50 vertical levels, while the GEOS-Chem Classic nested-grid simulation has 47 vertical levels. The WRF-GC model simulates meteorology online (2-min dynamical time step), while the GEOS-Chem Classic nested-grid simulation reads archived GEOS-FP assimilated meteorological dataset (`https://gmao.gsfc.nasa.gov/GMAO_products/`) and calculates advection at 5-min time step. All simulations use the same emissions, the same chemical module (GEOS-Chem column model), and identical chemical time steps. All simulations are performed on the same single-node hardware with 24 Intel Cascade Lake physical cores, 100 GB of RAM, and a networked Lustre high-performance file system. WRF-GC uses MPI parallelization, while GEOS-Chem Classic uses OpenMP parallelization.

Table 3 compares the simulation wall times for the WRF-GC v2.0 model (with various chemical feedback options) and for the GEOS-Chem Classic nested-grid model. Similar to our previous diagnosis (Lin et al., 2020), a one-way WRF-GC simulation (15282 s) is 53% faster than a similarly-configured GEOS-Chem Classic nested-grid simulation (33601 s). The better computational performance of WRF-GC is due to its faster dynamic calculations and its more

efficient parallelization of the chemical processes (Lin et al., 2020). The wall times for the two-way WRF-GC simulations with various combinations of chemical feedbacks (ARI only, ACI only, and both ARI and ACI) are all less than 11 % higher than the wall time for the one-way simulation. As expected, the slightly longer wall times in simulations with chemical feedbacks are mostly associated with the the extra calculations within the WRF-GC Coupler. The ARI calculations incur more wall time increases than the ACI calculations do. For reasons yet unclear, the wall time for the simulation with ARI only (17002 s) is slightly longer than that for the simulation with both ARI and ACI (16153 s). Nevertheless, in all WRF-GC simulations the coupling calculations are computationally economical and consume less than 9 % of the total wall times.

Table 3: Wall times of simulations conducted with the WRF-GC v2.0 model and the GEOS-Chem Classic nested-grid model (unit: s).

Model	**WRF-GC v2.0**				**GEOS-Chem Classic nested grid**
Experiment	One-way	ARI only	ACI only	ARI and ACI	v12.7.2
Total wall time	15378	17002	15283	16153	33601
Breakdown: WRF	7766	8374	7274	7511	-
Breakdown: GEOS-Chem	7242	7242	7591	7206	-
Breakdown: WRF-GC Coupler	370	1391	417	1436	-

References

Allen, D. J., Rood, R. B., Thompson, A. M., and Hudson, R. D.: Three-dimensional radon 222 calculations using assimilated meteorological data and a convective mixing algorithm, J. Geophys. Res. Atmos., 101, 6871–6881, https://doi.org/10.1029/95JD03408, 1996.

Baklanov, A., Schluenzen, K., Suppan, P., Baldasano, J., Brunner, D., Aksoyoglu, S., Carmichael, G., Douros, J., Flemming, J., Forkel, R., Galmarini, S., Gauss, M., Grell, G., Hirtl, M., Joffre, S., Jorba, O., Kaas, E., Kaasik, M., Kallos, G., Kong, X., Korsholm, U., Kurganskiy, A., Kushta, J., Lohmann, U., Mahura, A., Manders-Groot,

A., Maurizi, A., Moussiopoulos, N., Rao, S. T., Savage, N., Seigneur, C., Sokhi, R. S., Solazzo, E., Solomos, S., Sorensen, B., Tsegas, G., Vignati, E., Vogel, B., and Zhang, Y.: Online coupled regional meteorology chemistry models in Europe: current status and prospects, Atmos. Chem. Phys., 14, 317–398, https://doi.org/10.5194/acp-14-317-2014, 2014.

Byun, D. and Schere, K. L.: Review of the governing equations, computational algorithms, and other components of the Models-3 Community Multiscale Air Quality (CMAQ) modeling system, Appl. Mech. Rev., 59, 51–77, https://doi.org/10.1115/1.2128636, 2006.

Chen, F. and Dudhia, J.: Coupling an advanced land surface-hydrology model with the Penn State-NCAR MM5 modeling system. Part I: Model implementation and sensitivity, Mon. Weather Rev., 129, 569–585, https://doi.org/10.1175/1520-0493(2001)129<0569:CAALSH>2.0.CO;2, 2001a.

Chen, F. and Dudhia, J.: Coupling an advanced land surface-hydrology model with the Penn State-NCAR MM5 modeling system. Part II: Preliminary model validation, Mon. Weather Rev., 129, 587–604, https://doi.org/10.1175/1520-0493(2001)129<0587:CAALSH>2.0.CO;2, 2001b.

Chou, M. D. and Suarez, M. J.: An efficient thermal infrared radiation parameterization for use in general circulation models, NASA Tech. Memo., 104506, 3, 85pp, 1994.

Curci, G., Hogrefe, C., Bianconi, R., Im, U., Balzarini, A., Baró, R., Brunner, D., Forkel, R., Giordano, L., Hirtl, M., Honzak, L., Jiménez-Guerrero, P., Knote, C., Langer, M., Makar, P., Pirovano, G., Pérez, J., San José, R., Syrakov, D., Tuccella, P., Werhahn, J., Wolke, R., Žabkar, R., Zhang, J., and Galmarini, S.: Uncertainties of simulated aerosol optical properties induced by assumptions on aerosol physical and chemical properties: An AQMEII-2 perspective, Atmos. Environ., 115, 541 – 552, https://doi.org/10.1016/j.atmosenv.2014.09.009, 2015.

Eastham, S. D., Long, M. S., Keller, C. A., Lundgren, E., Yantosca, R. M., Zhuang, J., Li, C., Lee, C. J., Yannetti, M., Auer, B. M., Clune, T. L., Kouatchou, J., Putman, W. M., Thompson, M. A., Trayanov, A. L., Molod, A. M., Martin,

R. V., and Jacob, D. J.: GEOS-Chem High Performance (GCHP v11-02c): a next-generation implementation of the GEOS-Chem chemical transport model for massively parallel applications, Geosci. Model. Dev., 11, 2941–2953, https://doi.org/10.5194/gmd-11-2941-2018, 2018.

Eck, T., Holben, B., Reid, J., Dubovik, O., Smirnov, A., O'Neill, N., Slutsker, I., and Kinne, S.: Wavelength dependence of the optical depth of biomass burning, urban, and desert dust aerosols, J. Geophys. Res. Atmos., 104, 31 333–31 349, https://doi.org/10.1029/1999JD900923, 1999.

Fassi-Fihri, A., Suhre, K., and Rosset, R.: Internal and external mixing in atmospheric aerosols by coagulation: Impact on the optical and hygroscopic properties of the sulphate-soot system, Atmos. Environ., 31, 1393 – 1402, https://doi.org/10.1016/S1352-2310(96)00341-X, 1997.

Flemming, J., Inness, A., Flentje, H., Huijnen, V., Moinat, P., Schultz, M. G., and Stein, O.: Coupling global chemistry transport models to ECMWF's integrated forecast system, Geosci. Model. Dev., 2, 253–265, https://doi.org/10.5194/gmd-2-253-2009, 2009.

Gan, C. M., Pleim, J., Mathur, R., Hogrefe, C., Long, C. N., Xing, J., Wong, D., Gilliam, R., and Wei, C.: Assessment of long-term WRF–CMAQ simulations for understanding direct aerosol effects on radiation "brightening" in the United States, Atmos. Chem. Phys., 15, 12 193–12 209, https://doi.org/10.5194/acp-15-12193-2015, 2015.

Gao, Y., Zhao, C., Liu, X., Zhang, M., and Leung, L. R.: WRF-Chem simulations of aerosols and anthropogenic aerosol radiative forcing in East Asia, Atmos. Environ., 92, 250–266, https://doi.org/10.1016/j.atmosenv.2014.04.038, 2014.

Grell, G. A. and Freitas, S. R.: A scale and aerosol aware stochastic convective parameterization for weather and air quality modeling, Atmos. Chem. Phys., 14, 5233–5250, https://doi.org/10.5194/acp-14-5233-2014, 2014.

Holben, B., Eck, T., Slutsker, I., Tanre, D., Buis, J., Setzer, A., Vermote, E., Reagan, J., Kaufman, Y., Nakajima, T., Lavenu, F., Jankowiak, I., and Smirnov, A.: AERONET - A federated instrument network and data archive

for aerosol characterization, Remote Sens. Environ., 66, 1–16, https://doi.org/10.1016/S0034-4257(98)00031-5, 1998.

Hong, S.-Y., Noh, Y., and Dudhia, J.: A New Vertical Diffusion Package with an Explicit Treatment of Entrainment Processes, Mon. Weather Rev., 134, 2318–2341, https://doi.org/10.1175/MWR3199.1, 2006.

Iacono, M. J., Delamere, J. S., Mlawer, E. J., Shephard, M. W., Clough, S. A., and Collins, W. D.: Radiative forcing by long-lived greenhouse gases: Calculations with the AER radiative transfer models, J. Geophys. Res. Atmos., 113, https://doi.org/10.1029/2008JD009944, 2008.

Jimenez, P. A., Dudhia, J., Gonzalez-Rouco, J. F., Navarro, J., Montavez, J. P., and Garcia-Bustamante, E.: A Revised Scheme for the WRF Surface Layer Formulation, Mon. Weather Rev., 140, 898–918, https://doi.org/10.1175/MWR-D-11-00056.1, 2012.

Kaminski, J. W., Neary, L., Struzewska, J., McConnell, J. C., Lupu, A., Jarosz, J., Toyota, K., Gong, S. L., Côté, J., Liu, X., Chance, K., and Richter, A.: GEM-AQ, an on-line global multiscale chemical weather modelling system: model description and evaluation of gas phase chemistry processes, Atmos. Chem. Phys., 8, 3255–3281, https://doi.org/10.5194/acp-8-3255-2008, 2008.

Keller, C. A., Long, M. S., Yantosca, R. M., Da Silva, A. M., Pawson, S., and Jacob, D. J.: HEMCO v1.0: a versatile, ESMF-compliant component for calculating emissions in atmospheric models, Geosci. Model Dev., 7, 1409–1417, https://doi.org/10.5194/gmd-7-1409-2014, 2014.

Li, Z., Guo, J., Ding, A., Liao, H., Liu, J., Sun, Y., Wang, T., Xue, H., Zhang, H., and Zhu, B.: Aerosol and boundary-layer interactions and impact on air quality, Natl. Sci. Rev., 4, 810–833, https://doi.org/10.1093/nsr/nwx117, 2017.

Lin, H., Feng, X., Fu, T.-M., Tian, H., Ma, Y., Zhang, L., Jacob, D. J., Yantosca, R. M., Sulprizio, M. P., Lundgren, E. W., Zhuang, J., Zhang, Q., Lu, X., Zhang, L., Shen, L., Guo, J., Eastham, S. D., and Keller, C. A.: WRF-GC (v1.0): online coupling of WRF (v3.9.1.1) and GEOS-Chem (v12.2.1) for regional atmospheric chemistry

modeling – Part 1: Description of the one-way model, Geosci. Model Dev., 13, 3241–3265, https://doi.org/10.5194/gmd-13-3241-2020, 2020.

Lin, H., Jacob, D. J., Lundgren, E. W., Sulprizio, M. P., Keller, C. A., Fritz, T. M., Eastham, S. D., Emmons, L. K., Campbell, P. C., Baker, B., Saylor, R. D., and Montuoro, R.: Harmonized Emissions Component (HEMCO) 3.0 as a versatile emissions component for atmospheric models: application in the GEOS-Chem, NASA GEOS, WRF-GC, CESM2, NOAA GEFS-Aerosol, and NOAA UFS models, Geosci. Model Dev. Discuss., 2021, 1–26, https://doi.org/10.5194/gmd-2021-130, URL https://gmd.copernicus.org/preprints/gmd-2021-130/, 2021.

Lin, J.-T. and McElroy, M. B.: Impacts of boundary layer mixing on pollutant vertical profiles in the lower troposphere: Implications to satellite remote sensing, Atmos. Environ., 44, 1726–1739, 2010.

Long, M. S., Yantosca, R., Nielsen, J. E., Keller, C. A., da Silva, A., Sulprizio, M. P., Pawson, S., and Jacob, D. J.: Development of a grid-independent GEOS-Chem chemical transport model (v9-02) as an atmospheric chemistry module for Earth system models, Geosci. Model Dev., 8, 595–602, https://doi.org/10.5194/gmd-8-595-2015, 2015.

Lu, X., Hong, J., Zhang, L., Cooper, O. R., Schultz, M. G., Xu, X., Wang, T., Gao, M., Zhao, Y., and Zhang, Y.: Severe Surface Ozone Pollution in China: A Global Perspective, Environ. Sci. Technol. Lett., 5, 487–494, https://doi.org/10.1021/acs.estlett.8b00366, 2018.

Miao, Y. and Liu, S.: Linkages between aerosol pollution and planetary boundary layer structure in China, Sci. Total. Environ., 650, 288–296, https://doi.org/10.1016/j.scitotenv.2018.09.032, 2019.

Morrison, H., Thompson, G., and Tatarskii, V.: Impact of Cloud Microphysics on the Development of Trailing Stratiform Precipitation in a Simulated Squall Line: Comparison of One- and Two-Moment Schemes, Mon. Weather Rev., 137, 991–1007, https://doi.org/10.1175/2008MWR2556.1, 2009.

Nakanishi, M. and Niino, H.: An improved mellor-yamada level-3 model: Its numerical stability and application to a regional prediction of advection fog, Bound.-Lay. Meteorol., 119, 397–407, https://doi.org/10.1007/s10546-005-9030-8, 2006.

Renner, E. and Wolke, R.: Modelling the formation and atmospheric transport of secondary inorganic aerosols with special attention to regions with high ammonia emissions, Atmos. Environ., 44, 1904 – 1912, https://doi.org/10.1016/j.atmosenv.2010.02.018, 2010.

Tiedtke, M.: A comprehensive mass flux scheme for cumulus parameterization in large-scale models, Mon. Weather. Rev., 117, 1779–1800, https://doi.org/10.1175/1520-0493(1989)117<1779:ACMFSF>2.0.CO;2, 1989.

Wang, J., Wang, S., Jiang, J., Ding, A., Zheng, M., Zhao, B., Wong, D. C., Zhou, W., Zheng, G., Wang, L., Pleim, J. E., and Hao, J.: Impact of aerosol-meteorology interactions on fine particle pollution during China's severe haze episode in January 2013, Environ. Res. Lett., 9, https://doi.org/10.1088/1748-9326/9/9/094002, 2014.

Wang, Y., Yuan, Q., Shen, H., Zheng, L., and Zhang, L.: Investigating multiple aerosol optical depth products from MODIS and VIIRS over Asia: Evaluation, comparison, and merging, Atmos. Environ., 230, 117 548, https://doi.org/10.1016/j.atmosenv.2020.117548, 2020.

Wicker, L. J. and Skamarock, W. C.: Time-Splitting Methods for Elastic Models Using Forward Time Schemes, Mon. Weather Rev., 130, 2088–2097, https://doi.org/10.1175/1520-0493(2002)130<2088:TSMFEM>2.0.CO;2, 2002.

Witte, M. K., Yuan, T., Chuang, P. Y., Platnick, S., Meyer, K. G., Wind, G., and Jonsson, H. H.: MODIS Retrievals of Cloud Effective Radius in Marine Stratocumulus Exhibit No Significant Bias, Geophys. Res. Lett., 45, 10,656–10,664, https://doi.org/10.1029/2018GL079325, 2018.

Wolke, R., Knoth, O., Hellmuth, O., Schröder, W., and Renner, E.: The parallel model system LM-MUSCAT for

chemistry-transport simulations: Coupling scheme, parallelization and applications, Adv. Par. Com., 13, 363–369, https://doi.org/10.1016/S0927-5452(04)80048-0, 2004.

Wong, D. C., Pleim, J., Mathur, R., Binkowski, F., Otte, T., Gilliam, R., Pouliot, G., Xiu, A., Young, J. O., and Kang, D.: WRF-CMAQ two-way coupled system with aerosol feedback: software development and preliminary results, Geosci. Model. Dev., 5, 299–312, https://doi.org/10.5194/gmd-5-299-2012, 2012.

Wu, L., Su, H., and Jiang, J. H.: Regional simulations of deep convection and biomass burning over South America: 2. Biomass burning aerosol effects on clouds and precipitation, J. Geophys. Res. Atmos., 116, https://doi.org/10.1029/2011JD016106, 2011.

Wu, S., Mickley, L. J., Jacob, D. J., Logan, J. A., Yantosca, R. M., and Rind, D.: Why are there large differences between models in global budgets of tropospheric ozone?, J. Geophys. Res. Atmos., 112, https://doi.org/10.1029/2006JD007801, 2007.

Xing, J., Mathur, R., Pleim, J., Hogrefe, C., Gan, C.-M., Wong, D. C., Wei, C., and Wang, J.: Air pollution and climate response to aerosol direct radiative effects: A modeling study of decadal trends across the northern hemisphere, J. Geophys. Res. Atmos., 120, 12,221–12,236, https://doi.org/10.1002/2015JD023933, 2015.

Yan, H., Huang, J., Minnis, P., Yi, Y., Sun-Mack, S., Wang, T., and Nakajima, T. Y.: Comparison of CERES-MODIS cloud microphysical properties with surface observations over Loess Plateau, J. Quant. Spectrosc. Ra., 153, 65–76, https://doi.org/10.1016/j.jqsrt.2014.09.009, 2015.

Yu, S., Mathur, R., Pleim, J., Wong, D., Gilliam, R., Alapaty, K., Zhao, C., and Liu, X.: Aerosol indirect effect on the grid-scale clouds in the two-way coupled WRF-CMAQ: model description, development, evaluation and regional analysis, Atmos. Chem. Phys., 14, 11 247–11 285, https://doi.org/10.5194/acp-14-11247-2014, 2014.

Zhang, C. and Wang, Y.: Projected future changes of tropical cyclone activity over the western North and

South Pacific in a 20-km-Mesh regional climate model, J. Climate, 30, 5923–5941, https://doi.org/10.1175/JCLI-D-16-0597.1, 2017.

Zhang, C., Wang, Y., and Hamilton, K.: Improved representation of boundary layer clouds over the southeast Pacific in ARW-WRF using a modified Tiedtke cumulus parameterization scheme, Mon. Weather Rev., 139, 3489–3513, https://doi.org/10.1175/MWR-D-10-05091.1, 2011.

Zhang, X., Zhang, Q., Hong, C., Zheng, Y., Geng, G., Tong, D., Zhang, Y., and Zhang, X.: Enhancement of PM2.5 Concentrations by Aerosol-Meteorology Interactions Over China, J. Geophys. Res. Atmos., 123, 1179–1194, https://doi.org/10.1002/2017JD027524, 2018.

Zhang, Y., Zhang, X., Wang, L., Zhang, Q., Duan, F., and He, K.: Application of WRF/Chem over East Asia: Part I. Model evaluation and intercomparison with MM5/CMAQ, Atmos. Environ., 124, 285–300, https://doi.org/10.1016/j.atmosenv.2015.07.022, 2016.

Zhao, B., Liou, K.-N., Gu, Y., Li, Q., Jiang, J. H., Su, H., He, C., Tseng, H.-L. R., Wang, S., Liu, R., Qi, L., Lee, W.-L., and Hao, J.: Enhanced PM2.5 pollution in China due to aerosol-cloud interactions, Sci. Rep., 7, https://doi.org/10.1038/s41598-017-04096-8, 2017.